ACSNANO

www.acsnano.org

ARTICLE

Large-Scale Electric-Field Confined Silicon with Optimized Charge-Transfer Kinetics and Structural Stability for High-Rate Lithium-Ion Batteries

Tao Meng, Bo Li, Qiushi Wang, Junnan Hao, Binbin Huang, Feng Long Gu,* Huimin Xu, Peng Liu, and Yexiang Tong*

Cite This: *ACS Nano* 2020, 14, 7066–7076

Read Online

ACCESS | Metrics & More | Article Recommendations | Supporting Information

ABSTRACT: The stereospecific design of the interface effects can optimize the electron/Li-ion migration kinetics for energy-storage materials. In this study, an electric field was introduced to silicon-based materials (C-SiO_x@Si/rGO) through the rational construction of multi-heterostructures. This was achieved by manipulating the physicochemical properties at the atomic level of advanced Li-ion batteries (LIBs). The experimental and density functional theory calculations showed that the unbalanced charge distribution generated a large potential difference, which in turn induced a large-scale electric-field response with a boosted interfacial charge transfer in the composite. The as-prepared C-SiO_x@Si/rGO anode showed advanced rate capability (*i.e.*, 1579.0 and 906.5 mAh g^{-1} at 1000 and 8000 mA g^{-1}, respectively) when the migration paths of the Li-ion/electrons hierarchically optimized the large electric field. Furthermore, the C-SiO_x@Si/rGO composite with a high SiO_x@Si mass ratio (73.5 wt %) demonstrated a significantly enhanced structural stability with a 40% volume expansion. Additionally, when coupled with the $LiNi_{0.8}Co_{0.1}Mn_{0.1}O_2$ (NCM) cathode, the NCM//C-SiO_x@Si/rGO full cell delivers superior Li-ion storage properties with high reversible capacities of 157.6 and 101.4 mAh g^{-1} at 500 and 4000 mA g^{-1}, respectively. Therefore, the electric-field introduction using optimized electrochemical reaction kinetics can assist in the construction of other high-performance LIB materials.

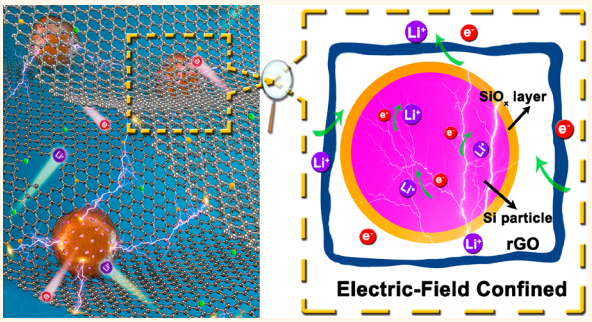

KEYWORDS: *interface effects, electric field, silicon-based materials, charge redistribution, density functional theory, Li-ion storage properties*

A need exists to develop alternative energy-storage systems because of the continued fossil energy consumption and resulting environmental deterioration. Rechargeable lithium-ion batteries (LIBs) are considered one of the most reliable devices for energy storage and conversion. Extensive interest in advanced portable electronics and electric vehicles requires achieving high-rate and very safe next-generation LIB technology.[1] Compared to the traditional graphite anode, silicon (Si) is abundant in nature and has several advantages. The theoretical capacity ($Li_{22}Si_5$, 4200 mAh g^{-1}) of Si is approximately 11 times larger than that of graphite (372 mAh g^{-1}). Furthermore, the volume metric capacity of Si (2081 mAh cm^{-3}) is significantly higher than that of graphite (779 mAh cm^{-3}).[2] Therefore, it is important to develop high-performance Si anodes for advanced LIBs. However, a Si anode is heavily restricted by its intrinsic defects. The crystalline Si tolerates a significant volume expansion (>300%) during lithiation−delithiation processes, which allows for mechanical fracture and structural collapse, leading to electrical open circuits and a rapid capacity decay. Furthermore, Si-based materials suffer from sluggish reaction kinetics because of low conductivity.[3] These intrinsic defects

Received: March 1, 2020
Accepted: May 13, 2020
Published: May 13, 2020

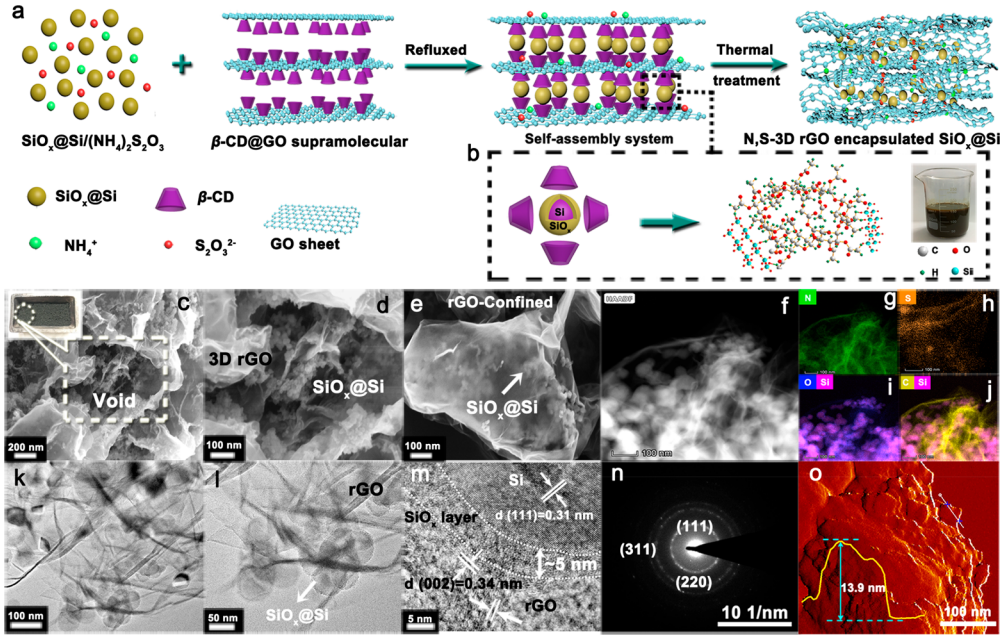

Figure 1. (a) Schematic illustration of the preparation of the C-SiO$_x$@Si/rGO composite. (b) Possible structure of β-CD/SiO$_x$. (c–e) SEM images, (f–j) HAADF images with the corresponding EDX mapping, (k, l) TEM images, (m) HRTEM image, (n) SAED pattern, and (o) AFM image of the C-SiO$_x$@Si/rGO composite.

greatly limit the use of Si materials in energy-storage applications.

Extensive efforts have been made to address these challenges, including nanostructure morphology synthesis,[4] conductive coating materials,[5] and developing binders.[6] These advancements have achieved improved electrochemical performance when compared to bulk Si. An effective strategy for constructing silicon–carbon (Si–C) nanostructure composites is to use the carbon matrix to enhance the electrical conductivity and create an additional buffer space to support the large volumetric strain. Reduced graphene oxide (rGO) is a promising carbon matrix used to modify the physicochemical properties of Si, owing to its advanced electrical conductivity, high specific area, and mechanical strength.[7] Ruoff *et al.* fabricated a three-dimensional (3D) electrode through drop-casting an rGO-coated Si composite onto graphite foam. The electrode delivered a sufficient reversible capacity of 983 mAh g^{-1} at 400 mA g^{-1} and retained 370 mAh g^{-1} after 100 cycles.[8] Cui *et al.* encapsulated micro-Si particles using conformal rGO cages. The Coulombic efficiency and solid electrolyte interface (SEI) stability were significantly improved owing to the extra voids combined with graphitic carbon.[9] However, the synthesis processes used in these methods are relatively expensive and difficult to scale. Furthermore, previous studies have not shown in-detail investigations regarding the physicochemical behavior between the different components in the Si-based composite. This leads to an insufficient utilization of the active material. Subsequently, the improved performance does not effectively use the large theoretical capacity of Si. Therefore, a need exists to effectively solve the Si bottleneck to develop high-rate and high-energy-density LIBs.

Recent studies have demonstrated that the electrochemical behavior can be effectively manipulated through regulating the interfacial interaction in the composite. In our previous work, a flexible LIB was designed using a gravimetric energy density of 314 Wh kg^{-1} through establishing the interaction between the flexible carbon cloth and $NiCo_2O_4$.[10] Yu *et al.* synthesized the C-doped Co_3O_4 nanocrystal composite using local electric-field effects *via* manipulating an imbalanced charge distribution. The as-prepared electrode showed an advanced Li-ion storage property of 950 mAh g^{-1} after 300 cycles at 0.5 A g^{-1}.[11] These improvements in electrochemical performance meet the Si anode requirements. When considering the natural defects of Si, it is important to establish a clear connection between the different components by combining structural features, to explore highly efficient Si anodes.

This study successfully applied a large-scale electric field to Si-based materials using optimized charge-transfer kinetics and structural stability. SiO$_x$@Si particles were oriented and encapsulated into a 3D nitrogen (N)- and sulfur (S)-doped rGO using a supramolecular self-assembly process. The heterogeneous interface configuration limited the expansion of Si and created a strong charge interaction between the different components. A large-scale electric field was constructed *in situ* in the regions where SiO$_x$@Si was limited by rGO. This provided a strong driving force for rapid ion/electron migration. The as-prepared C-SiO$_x$@Si/rGO anode showed excellent Li-ion storage properties, which alleviated volume expansion. When coupled with the Li-$Ni_{0.8}Co_{0.1}Mn_{0.1}O_2$ (NCM) cathode, the full cell delivers excellent rate capability. This modulation strategy provides a promising method to develop high-performance LIBs for practical applications.

RESULTS AND DISCUSSION

The synthesis process of the C-SiO$_x$@Si/rGO composite is presented in Figure 1a. According to previous reports, graphite oxide (GO) and β-cyclodextrin (β-CD) tend to form a supramolecular self-assembly system after ultrasonic treatment.[12] This creates a stable space for the intercalation of Si into the GO sheets. During the annealing process, ammonium thiosulfate ($(NH_4)_2S_2O_3$) was used as the foaming agent to create a loose and adaptable inner 3D structure with abundant reserved voids for rGO. A proportion of N and S was

https://dx.doi.org/10.1021/acsnano.0c01796
ACS Nano 2020, 14, 7066–7076

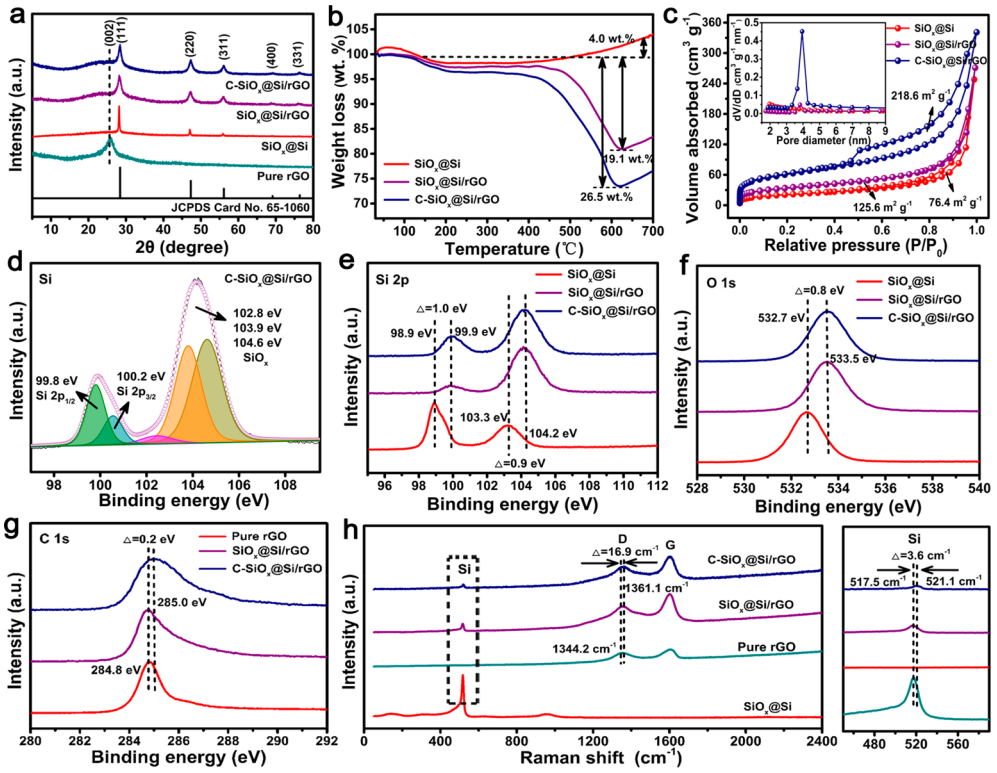

Figure 2. Structural and compositional characterization of the as-prepared samples. (a) XRD patterns, (b) TGA curves, (c) N_2 adsorption/desorption isotherms, and pore size distribution of the as-prepared materials. (d) High-resolution XPS Si spectrum of the SiO_x@Si/rGO composite. XPS spectra of (e) Si 2p and (f) O 1s of SiO_x@Si, SiO_x@Si/rGO, and C-SiO_x@Si/rGO. (g) C 1s of pure rGO, SiO_x@Si/rGO, and C-SiO_x@Si/rGO. (h) Raman spectra of pure rGO, SiO_x@Si, SiO_x@Si/rGO, and C-SiO_x@Si/rGO.

successfully transferred into the internal structure. The Fourier transform infrared spectroscopy (FTIR) test results (Figure S1) showed that C−H asymmetric stretching vibrations appeared at 2920 cm^{-1} in the β-CD/SiO_x@Si composite. The strength of Si−H_x stretching modes (2100 cm^{-1}) in β-CD/SiO_x@Si was significantly lower than that in SiO_x@Si. This indicates that β-CD was successfully grafted onto the SiO_x surface.[13,14] More importantly, the O−H stretching vibration peak (~3330 cm^{-1}) in β-CD/SiO_x@Si shifted toward low wave when compared to β-CD and SiO_x@Si (~3420 cm^{-1}). This suggests that SiO−H was formed between SiO_x and β-CD.[15,16] A possible molecular structure is shown in Figure 1b. Additionally, the resulting SiO_x@Si particle surface has abundant functional groups (*i.e.*, −OH) because pure Si has been treated using a piranha solution. The functional groups can form a hydrogen bond with −COOH in GO.[6] Therefore, SiO_x@Si, β-CD and GO were combined using the chemical interactions mentioned above. The structure and morphology of the synthesized samples were characterized using a field-emission scanning electron microscope (FESEM). Figure 1c and d show that the SiO_x@Si particles were well-encapsulated by the 3D rGO and created a controllable buffer void. The 3D morphology of rGO significantly increased the encapsulation probability of the SiO_x@Si particles. Figure 1e shows that the SiO_x@Si was well confined within the 3D rGO matrix, resulting in a direct contact of each component. The SiO_x@Si particles (~50 nm) were randomly agglomerated in the SiO_x@Si sample (Figure S2a−c). The SiO_x@Si in SiO_x@Si/rGO was exposed because of the absence of β-CD. Therefore, SiO_x@Si simply adhered to the rGO surface (Figures S2d−f). Energy-dispersive X-ray spectroscopy (EDX) mapping was performed to examine the distribution of rGO sheets and SiO_x@Si particles. Figure 1g and h show that a proportion of N (3.81%) and that of S (0.62%) were successfully doped into the rGO sheets. The distributions of O and Si were consistent (Figure 1i), indicating that an adequate oxidation layer (SiO_x) covered the Si surface. The distributions of C and Si are visible (Figure 1j), which substantiates that the SiO_x@Si particles were encapsulated by the 3D rGO.

The transmission electron microscope (TEM) images of the C-SiO_x@Si/rGO composite showed that the SiO_x@Si particles were firmly intertwined by rGO without aggregation (Figure 1k and l). The 0.31 nm lattice fringe of the (111) plane attributed to Si particles can be clearly observed in high-resolution TEM (HRTEM, Figure 1m). The amorphous SiO_x layer (~5 nm) was next to the Si, and the outermost layer of the fringe band (0.34 nm) was assigned to rGO. Therefore, the heterostructure containing rGO//SiO_x and SiO_x//Si hetero-interfaces was successfully fabricated, which is highly identified with the SEM results. The interface engineering will be responsible for the optimized Li-ion transfer properties. The TEM and HRTEM images of SiO_x@Si and SiO_x@Si/rGO are given in Figure S3. The selected-area electron diffraction (SAED) patterns of SiO_x@Si (Figure S3d), SiO_x@Si/rGO (Figure S3h), and C-SiO_x@Si/rGO (Figure 1n) confirmed the obtained samples are composed of crystalline Si. An accurate rGO thickness measurement of 13.9 nm was obtained (Figure 1o).

The X-ray diffraction (XRD) patterns of the Si-based materials demonstrated that all characteristic peaks were well-matched with crystalline Si (JCPDS Card No. 65-1060). Additionally, a broad peak appeared on the left of the (111)

https://dx.doi.org/10.1021/acsnano.0c01796
ACS Nano 2020, 14, 7066−7076

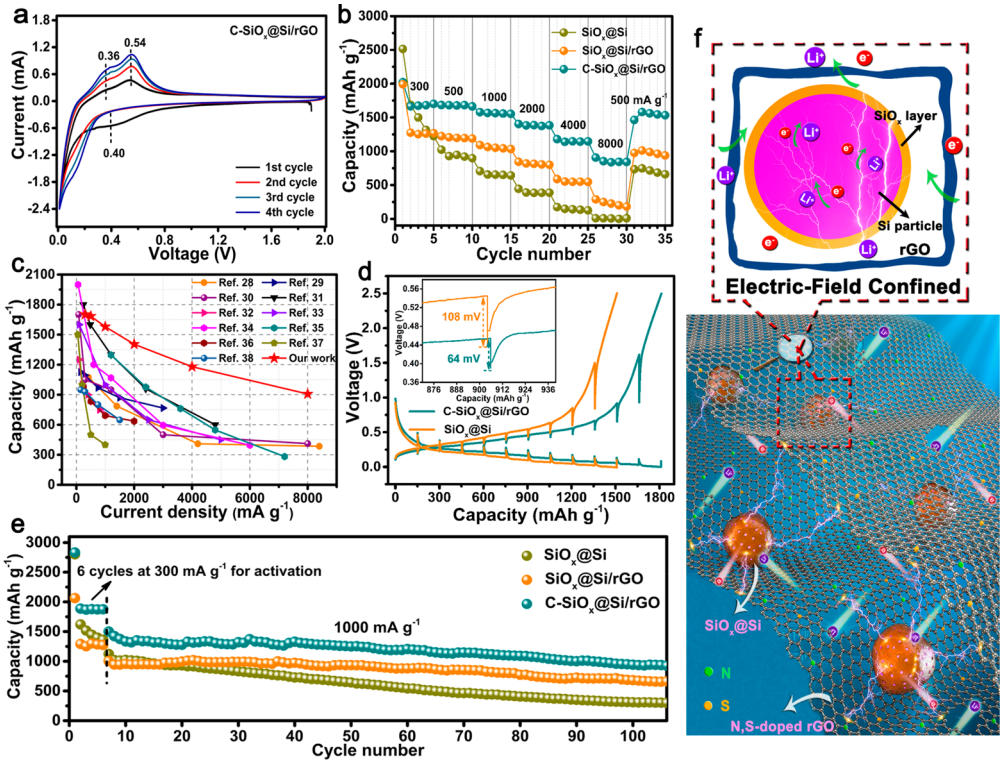

Figure 3. Half-cell electrochemical performance of as-prepared electrodes. (a) CV curves of C-SiO_x@Si/rGO electrodes at 0.2 mV s^{-1}. (b) Rate performance. (c) Comparisons between the rate performances of C-SiO_x@Si/rGO electrodes and the reported Si-based electrodes. (d) GITT measurements of SiO_x@Si and C-SiO_x@Si/rGO electrodes. (e) Cycle performance at 1000 mA g^{-1}. (f) Schematic description of the electric field in the C-SiO_x@Si/rGO composite.

plane, which is associated with the carbon matrix phase located in the (002) plane (Figure 2a).[17] Thermal gravimetric analysis (TGA) revealed that the carbon contents in SiO_x@Si/rGO and C-SiO_x@Si/rGO composites were 19.1 and 26.5 wt %, respectively (Figure 2b). The TGA curves of the three samples increased in the final stage (~4.0 wt %) owing to the oxidation of Si. The nitrogen (N_2) adsorption/desorption measurement results suggested that the C-SiO_x@Si/rGO composite had the largest specific surface (218.6 m^2 g^{-1}) with a ~4 nm pore diameter (Figure 2c). The hierarchically porous structure primarily resulted from the gas-foaming effect and N and S co-doping in the 3D rGO. This increased the surface area available for electrolyte infiltration and allowed the rapid transfer of Li ions.

X-ray photoelectron spectroscopy (XPS) measurement was adopted to verify the valence state and composition of the composites (Figure S4). The Si spectra of C-SiO_x@Si/rGO can be divided into two main parts (Figure 2d). Namely, the binding energy peaks at approximately 99.8 (Si $2p_{1/2}$) and 100.2 eV (Si $2p_{3/2}$), which are characteristic peaks of crystalline Si, and the peaks at 102.8, 103.9, and 104.6 eV, which are SiO_x peaks.[18] The SiO_x peaks in SiO_x@Si/rGO (Figure S5b) and C-SiO_x@Si/rGO were stronger than that in SiO_x@Si (Figure S5a), indicating that thicker SiO_x layers were formed during the thermal treatment process. The detailed analysis revealed that the binding energies of different elements experienced various degrees of deviation. For instance, the crystalline Si and SiO_x peaks for SiO_x@Si/rGO and C-SiO_x@Si/rGO shifted by 1.0 and 0.9 eV compared to SiO_x@Si (Figure 2e). The O 1s peaks of SiO_x@Si/rGO and C-SiO_x@Si/rGO also shifted toward higher binding energy, with a difference of 0.8 eV (Figure 2f). C-SiO_x@Si/rGO became wider for the C 1s spectra and shifted by 0.2 eV relative to SiO_x@Si and SiO_x@Si/rGO (Figure 2g). The shifted binding energy of the C-SiO_x@Si/rGO composite indicates the occurrence of charge interaction and imbalanced charge distribution.[10,19,20] Furthermore, as shown in Figure 2h, Raman spectroscopy showed the deviated Si and D peaks (3.6 and 16.9 cm^{-1}, respectively) of the C-SiO_x@Si/rGO composite with respect to the strong electron interaction.[21] The analysis showed that the imbalanced charge distribution of Si, O, and C occurred in the heterogeneous interfacial charge, creating an electric field in the C-SiO_x@Si/rGO composite.[20]

The N spectra of SiO_x@Si/rGO and C-SiO_x@Si/rGO (Figure S6) can be divided into four primary peaks at 398.7, 400.3, 401.3, and 403.0 eV, assigned to pyridinic N, pyrrolic N, quaternary N, and *N*-oxide, respectively.[22] The high-resolution S 2p spectrum suggests three peaks at 163.9, 165.0 (C−S−C), and 168.7 eV (C−SO_x−C), which are covalent bonds between thiophene-S and different oxidized sulfur bond groups (Figure S7).[23] Ion doping leads to a lopsided charge distribution near the doping sites and extends the effective range of the electric field.[11] Particularly, the pyrrolic N experiences rapid charge diffusion and favorable electron donor or acceptor properties, facilitating effective electron-transfer reactions. The pyridinic N has a pair of electrons that couple with the *p*-conjugated rings, which leads to the excellent electron acceptor/donor properties and Faradaic pseudocapacitance.[24,25] The electron paramagnetic resonance (EPR) measurement results revealed that the C-SiO_x@Si/rGO composite had abundant oxygen vacancies with the strongest signal peak at g = 2.0 (Figure S8).[26,27] The addition of 3D rGO increased the bonding probability of C and O during the thermal process, resulting in the largest number of oxygen vacancies in the C-SiO_x@Si/rGO

https://dx.doi.org/10.1021/acsnano.0c01796
ACS Nano 2020, 14, 7066−7076

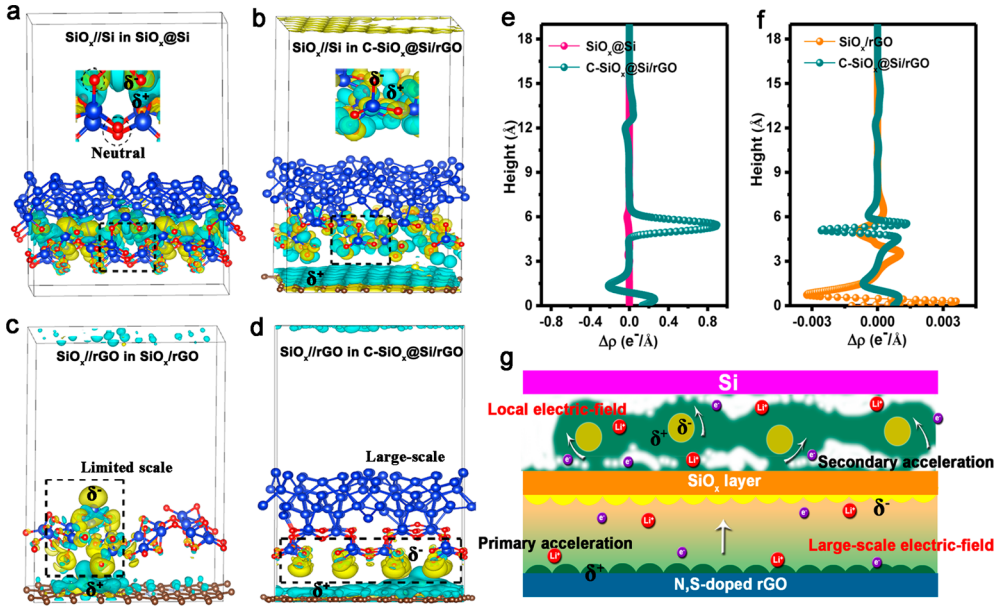

Figure 4. Theoretical calculations of charge density distribution for the SiO_x//Si heterojunction in (a) SiO_x@Si and (b) C-SiO_x@Si/rGO models. SiO_x//rGO heterojunction in (c) SiO_x/rGO and (d) C-SiO_x@Si/rGO models (yellow indicates charge accumulation, while green indicates depletion). The planar-averaged electron density difference $\Delta\rho$ for (e) SiO_x//Si and (f) SiO_x//rGO. (g) Schematic description of paths for Li-ion and electron migration at the heterointerfaces in the electric field.

composite.[19] The unsaturated states of the surface O, created by the amorphous SiO_x, modulated the electrical ordering on the nanoscale and enhanced the electric-field effect. This provided opportunities to modify the electronic structure and boost the interfacial charge migration rate for Li-ion storage capability.

Figure 3a shows the representative cyclic voltammetry (CV) behavior of the C-SiO_x@Si/rGO electrode for the first four cycles. A broad peak was formed near 0.40 V during the initial charge process, corresponding to the growth of the SEI film and the lithiation process of the SiO_x layers.[6] Increased scanning generated a pair of oxidation peaks near 0.36 and 0.54 V, attributed to the Li dealloying process of Li−Si phases to Si domains. The CV curves of SiO_x@Si and SiO_x@Si/rGO electrodes are presented in Figure S9. When the scan rate was increased to 1.6 mV s^{-1}, the redox peak slightly shifted (Δ = 0.06 V), indicating the fast Li-ion diffusion and low polarization in the C-SiO_x@Si/rGO electrode (Figure S10). The rate performance was evaluated from 300 to 8000 mA g^{-1} (Figure 3b). The initial discharge capacities for SiO_x@Si, SiO_x@Si/rGO, and C-SiO_x@Si/rGO at 300 mA g^{-1} were 2515.4, 1992.4, and 2022.1 mAh g^{-1}, respectively. The initial Coulombic efficiency (ICE) of the C-SiO_x@Si/rGO electrode was 70.6%, while those of the SiO_x@Si and SiO_x@Si/rGO electrodes were 60.9% and 57.5%, respectively. After five cycles of activation, the capacity of C-SiO_x@Si/rGO was stabilized at 1701.4 mAh g^{-1}. The C-SiO_x@Si/rGO electrode had an advanced rate capability with higher capacities of 1684.3, 1579.0, 1404.4, and 1180.2 mAh g^{-1} at 500, 1000, 2000, and 4000 mA g^{-1}, respectively. Even at 8000 mA g^{-1}, a capacity of 906.5 mAh g^{-1} could be achieved. When the current density returned to 500 mA g^{-1}, the capacity are basically recovered. On the contrary, the SiO_x@Si electrode exhibited low kinetics and had capacity failure at 8000 mA g^{-1}. The rate performance comparison of this study with other reported Si-based anodes is shown in Figure 3c,[28−38] which indicates that excellent redox reaction kinetics were achieved in this study. The corresponding galvanostatic charge/discharge profiles of different electrodes are presented in Figure S11.

Additionally, the galvanostatic intermittent titration technique (GITT) measurement was performed to investigate the electrochemical reaction kinetics of the C-SiO_x@Si/rGO electrode (Figure 3d). The SiO_x@Si and C-SiO_x@Si/rGO electrodes were exposed to continuous lithiation−delithiation at 300 mA g^{-1} for 30 min. The batteries were left as an open circuit for 120 min to achieve an equilibrium potential. The C-SiO_x@Si/rGO electrode had the lowest voltage difference between the charge/discharge platform, indicating less polarization. The inset in Figure 3d reveals that the SiO_x@Si electrode had a large overpotential (108 mV), which was significantly higher than that of C-SiO_x@Si/rGO (64 mV). This indicates that the electrochemical reaction resistance of C-SiO_x@Si/rGO was lower than that of the SiO_x@Si electrodes.[39] Using the CV measurement results (Figures 3a and S9a),[19] the Li-ion diffusion coefficient of the C-SiO_x@Si/rGO electrode was calculated as 5.4×10^{-9} cm^2 s^{-1}. This result is more than eight times that obtained for SiO_x@Si (6.43×10^{-10} cm^2 s^{-1}). The enhanced mobility substantiated that the electric field facilitated the Li-ion diffusion rate. Consequently, hierarchically optimizing the ion/electron migratory pathways accelerated the dynamic redox reaction of the C-SiO_x@Si/rGO electrode.

A higher current density (1000 mA g^{-1}) was applied to the as-prepared electrodes to verify that the electric field in the SiO_x@Si particles remained robust (Figure 3e). After several activation cycles at 300 mA g^{-1}, a significant reversible capacity of 925.4 mAh g^{-1} was obtained for the C-SiO_x@Si/rGO electrode after 100 cycles. However, SiO_x@Si/rGO and SiO_x@Si anodes maintained low capacities of 662.5 and 300.4 mAh g^{-1}, respectively. The rapid capacity fading suggested that the SiO_x@Si electrode structure experienced severe disintegration during the Li-ion insertion/extraction processes. All electrodes showed excellent reversibility for Si, with Coulombic efficiency above 98% during cycling (Figure S12). Furthermore, an

https://dx.doi.org/10.1021/acsnano.0c01796
ACS Nano 2020, 14, 7066−7076

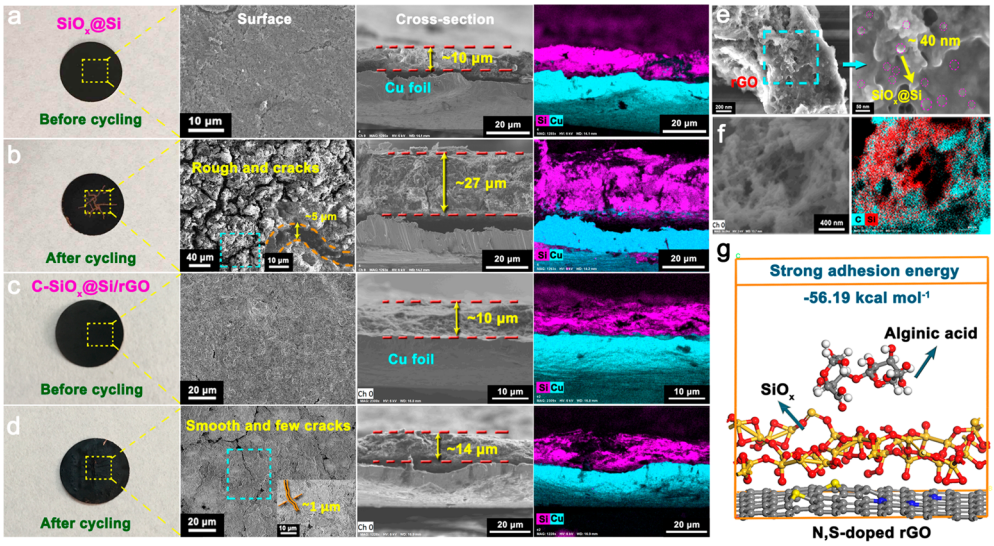

Figure 5. Compositional characterization and morphology of SiO_x@Si and C-SiO_x@Si/rGO after cycling. SEM images and EDS mapping of the surface and cross-section of SiO_x@Si and C-SiO_x@Si/rGO electrodes: (a, c) before cycling, (b, d) after cycling. (e, f) SEM images and EDS mapping of the C-SiO_x@Si/rGO composite. (g) DFT theoretical calculation of the interaction between C-SiO_x@Si/rGO and alginic acid.

adequate reversible capacity of 797.4 mAh g^{-1} could be obtained at 2 A g^{-1} after 350 cycles (Figure S13). The electrochemical impedance spectroscopy (EIS) test results confirmed that the C-SiO_x@Si/rGO electrode had a lower ion-diffusion resistance, revealing faster Li-ion transfer rates (Figure S14a). The corresponding EIS fitting line and equivalent circuit are shown in Figure S14b.

Figure 3f illustrates the electric field in the C-SiO_x@Si/rGO composite. The imbalanced charge distribution among the Si, SiO_x, and rGO interfaces generated an electric-field force, thereby significantly enhancing the high-rate capability through boosting the electron and Li-ion mobility between the current collector and active sites.[40,41] The configuration of SiO_x@Si combined with the well-connected 3D N,S-doped rGO networks activated more active sites and created a short diffusion pathway for the electron and Li-ion exchange for the SiO_x@Si nanoparticles, thereby accelerating the electron and Li-ion radial transport along the interlocked rGO, building an electrical superhighway. Therefore, the elastic rGO coating on the SiO_x@Si particles reduces volume variations and maintains the durability of the C-SiO_x@Si/rGO electrode. Furthermore, the electric field can guarantee structural integrity between different components and facilitate the redox reaction kinetics in the C-SiO_x@Si/rGO electrode.

Density functional theory (DFT) calculations were performed to investigate the unbalanced charge distribution at the heterogeneous atomic interface. The calculated results of SiO_x@Si revealed the charge density redistribution at the SiO_x//Si heterojunction interface. However, a large percentage of O atoms remained neutral and were not converted to the negative region (Figure 4a). After adding rGO to the model (C-SiO_x@Si/rGO), the charge rearranged at the SiO_x interface reappeared. Furthermore, the charge density distribution in the rGO layer plane was completely reduced. Moreover, the O atoms in the SiO_x layer transformed into a negative center surrounded by a positively charged region (Figure 4b). The curve of the planar-averaged electron density difference ($\Delta\rho$) in the SiO_x//Si heterojunction indicated that the charge density difference was more apparent and amplified in C-SiO_x@Si/rGO (Figure 4e). This assists in extending the local built-in electric field.[11,42] Only partial charge accumulation and depletion occurred in the SiO_x//rGO heterojunction in the confined area at the SiO_x//rGO heterointerface. This indicates that a limited electric field exists in the SiO_x/rGO model (Figure 4c). However, when Si atoms were added to the SiO_x/rGO model (C-SiO_x@Si/rGO), the charge distribution changed significantly. The charge density improved in the SiO_x layer plane and reduced on the rGO surface (Figure 4d). This extensive and structured charge-transfer behavior is advantageous when generating potential differences, thereby inducing a large-scale in-plane electric-field effect. The SiO_x//rGO heterojunction with the homogeneous space charge layer at the interface can significantly accelerate electron/ion-transfer kinetics.[40,43] The charge density variation curve of SiO_x//rGO is shown in Figure 4f. In conclusion, rGO, SiO_x, and Si were necessary to create a large-scale unbalanced charge distribution in the C-SiO_x@Si/rGO composite. This generated a powerful electric field through the synergistic effect of the abundant heterogeneous interface. These theoretically calculated results support those of the XPS and Raman tests.

Figure 4g is a schematic description of the Li-ion and electron migration paths at various interfaces during the discharge (insertion) process of the C-SiO_x@Si/rGO composite. The charge accumulation and depletion generated an extensive electric field with an adventitious strong Coulomb force. This points from the neutral area to the negatively charged area, providing the potential driving force for interfacial electron transport.[44] When Li-ions were placed in the extended electric field, the Li-ion transfer was boosted by the intense electric-field forces generated by the potential difference between rGO and SiO_x in the rGO//SiO_x heterojunction. After acceleration was sustained, the Li-ion and electron arrived at the SiO_x layer. They were released and diffused rapidly in different directions through the self-adaptive local electric field. This continued until they are transferred to the Si interface and obtained secondary acceleration. After full lithiation, the electronegative region gradually transformed into a neutral state. During the charging process, the electric-field

https://dx.doi.org/10.1021/acsnano.0c01796
ACS Nano 2020, 14, 7066−7076

force points from the positive region near the O and C to the electrically neutral area, facilitating the extraction of Li-ions.[42] The poor encapsulation of the SiO_x@Si/rGO composite by the rGO resulted in a reduction in the electric field and limited the electrochemical performance. To sum up, this flexible self-adaptive electric field affected the regulation strategy that assists in promoting the redox reaction of Li-ions in the electrode.

The different performance results obtained for cycle stability were investigated using SEM measurements of the SiO_x@Si and C-SiO_x@Si/rGO electrodes after cycling. The SEM and mapping images for the surface and cross-section showed significant changes in the electrodes before and after cycling. The surface of the SiO_x@Si electrode was rough and had large cracks (~5 μm, Figure 5b). Furthermore, the cross-sectional thickness of the SiO_x@Si electrode expanded from 10 μm to 27 μm (170% swelling). In contrast, the C-SiO_x@Si/rGO electrode had a smooth surface with minor cracks (~1 μm), and the active materials were not detached from the current collector. The electrode thickness increased from 10 μm to 14 μm with a 40% volume expansion (Figures 5c and d). The SiO_x@Si particles (~40 nm) were homogeneously distributed without significant pulverization and were still imprisoned by the rGO shell (Figure 5e). The elastic 3D rGO barrier firmly encapsulated the SiO_x@Si grains, protecting the SiO_x@Si particles from agglomeration and pulverization. However, the SiO_x@Si electrode did not perform that well (Figure S15). The mapping test results displayed that the distribution of Si was almost identical to that of C, thereby confirming that rGO effectively reduced the fractures of SiO_x@Si (Figure 5f). Raman test results verified that the Si signal existed in C-SiO_x@Si/rGO, indicating that the crystalline Si had not been converted to an amorphous state (Figure S16).

Another set of DFT calculations was performed to investigate the physical origin of the robust structure of the C-SiO_x@Si/rGO electrode. Based on the previous characterization results, the rGO sheet and SiO_x layer were in direct contact with sodium alginate. The first step of the electrode preparation involved dissolving and disassociating the sodium alginate into Na^+ and alginic acid. The optimized theoretical model is shown in Figure 5g. The calculated results suggested that alginic acid strongly interacted with C-SiO_x@Si/rGO (-56.19 kcal mol^{-1}) during the mixing process of the electrode fabrication. The strong interaction energy contributed to the complete combination of the binder and active materials, resulting in the structural integrity and prolonged cycling stability of the as-prepared C-SiO_x@Si/rGO electrode.[6,45] As illustrated in Figure S17, after the activation at a low current density, the SiO_x@Si particles became prone to pulverization during cycling. The SiO_x@Si electrodes lacked adaptable supporters and electric-field effects. Therefore, the SiO_x@Si electrodes incurred severe pulverization after cycling, leading to the structural collapse and subsequent electrical disconnect. In contrast, the loose internal structure created by the flexible rGO buffer layer restricted the significant volume change of SiO_x@Si in the C-SiO_x@Si/rGO electrode. In particular, the presence of the electric-field effect made the electrode structure more stable with considerable SiO_x@Si active material retained. The above characterization results can be summarized as follows: the well-established sufficient inner void regulates the volume expansion and is tolerant to mechanical stresses during the lithiation process, and the enlarged electric field is extremely advantageous to the structural stability of the Si-based electrode, thereby circumventing the volume change induced by instability during cycling.

A real-world application of the C-SiO_x@Si/rGO composite in LIBs was evaluated using a full cell configuration with the commercialized NCM as the cathode. Figure S18a is a simplified schematic illustration of the NCM//C-SiO_x@Si/rGO full cell. The corresponding redox reaction equation of the full cell is shown below:

$$Li[Ni_{0.8}Co_{0.1}Mn_{0.1}O_2] + [C\text{-}SiO_x@Si/rGO] \rightleftharpoons Li_{1-x}[Ni_{0.8}Co_{0.1}Mn_{0.1}O_2] + Li_x[C\text{-}SiO_x@Si/rGO] \quad (1)$$

To make full use of the NCM electrode in the full cell, the C-SiO_x@Si/rGO electrode was first prelithiated with Li foil (Figure S18b). The rate performance and CV curve of NCM are shown in Figure S19. The Li-ion storage behavior of the NCM//C-SiO_x@Si/rGO full cell was investigated using CV measurements from 0.2 to 2.0 mV s^{-1} with a cutoff voltage between 2.8 and 4.5 V (Figure 6a). The curves show three

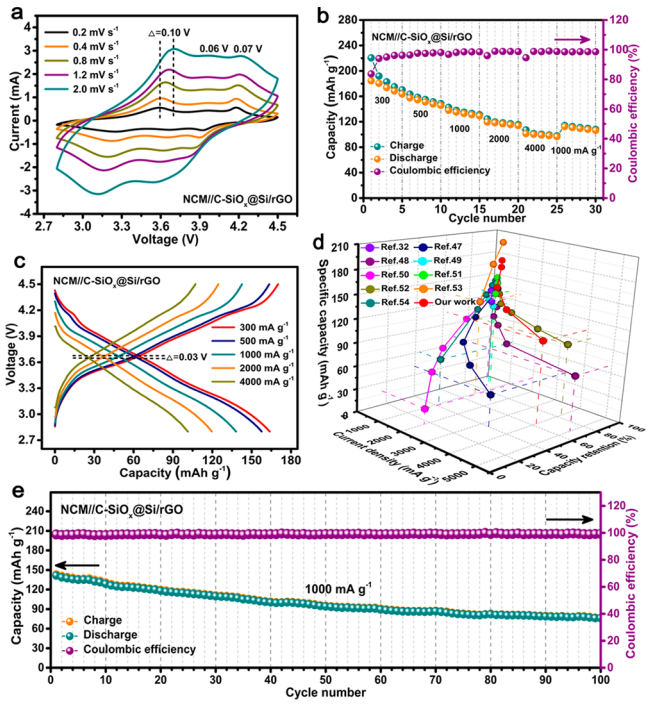

Figure 6. Electrochemical properties of the NCM//C-SiO_x@Si/rGO full cell. (a) CV curves at different scan rates. (b) Rate performance. (c) Galvanostatic charge/discharge curves. (d) Comparisons of rate performance of Si-based full cell with previous studies. (e) Cycle performance.

pairs of sharp and strong redox peaks, ascribed to the rapid kinetics of the Li^+ insertion/extraction reaction in the full cell. Additionally, the redox peaks remained undeformed (Δ = 0.10, 0.06, and 0.07 V) when the scan rate was increased to 2.0 mV s^{-1}. This indicates that a low polarization and stable reversible redox reaction occurred in the NCM//C-SiO_x@Si/rGO full cell. As shown in Figure 6b, the full cell maintained an excellent rate performance similar to that of the half-cell. The initial charge and discharge capacities of NCM//C-SiO_x@Si/rGO at 300 mA g^{-1} were 220.5 and 184.5 mAh g^{-1} with 83.7% ICE (Figure S20). After a five-cycle activation, a stable

https://dx.doi.org/10.1021/acsnano.0c01796
ACS Nano 2020, 14, 7066−7076

discharge capacity of 163.8 mAh g^{-1} was reached. At rates of 500, 1000, and 2000 mA g^{-1}, the NCM//C-SiO_x@Si/rGO full cell can deliver a high reversible capacity of 157.6, 138.1, and 119.6 mAh g^{-1}, respectively. Furthermore, a capacity of 101.4 mAh g^{-1} could be maintained at 4000 mA g^{-1}, corresponding to an energy density of 375.2 Wh kg^{-1}. The full cell recovered most of its capacity as the current rate returned to 1000 mA g^{-1}. The admirable rate capability of the full cell may be attributed to the relatively high capacitive contribution (Figure S21).[46] Moreover, the voltage profile of the NCM//C-SiO_x@Si/rGO full cell had an average voltage value of ~3.7 V, with only a 0.03 V voltage platforms shift from 300 to 4000 mA g^{-1} (Figure 6c). As shown in Figure 6d, the rate performance of Si-based full cells prepared in this study was superior to that reported in the literature.[32,47−54] This comparison was facilitated using a current density that was based on the mass of active materials in the anode. The comparative results indicated that the introduction of the electric field created an opportunity to construct advanced electrode materials. The excellent lithium-storage behavior resulted from the in-plane self-adaptive electric field, which was essential for boosting the interfacial charge migration and Li-ion transfer rates in the electrode. Additionally, the NCM//C-SiO_x@Si/rGO full cell exhibited outstanding cycling stability with a high reversible capacity of 141.5 mAh g^{-1} and a maintained a capacity of 76.1 mAh g^{-1} (281.6 Wh kg^{-1}) after 100 cycles at 1000 mA g^{-1} (Figure 6e). The Coulomb efficiency exceeded 99.0% throughout the cycling, highlighting the admirable reversibility of Li ions. The EIS of NCM//C-SiO_x@Si/rGO after cycling is shown in Figure S22, which nearly corresponds to the half-cell tests. The relatively low charge-transfer impedance of the NCM//C-SiO_x@Si/rGO full cell resulted in advantageous electrochemical properties. Figure S23 shows a photographic image of a screen with 57 LED elements lighted using the assembled full cell, indicating the potential in the energy-storage field.

CONCLUSION

This study described a rationally constructed abundant heterogeneous atomic interface *via* coupling different components in a C-SiO_x@Si/rGO composite and applied the electric-field concept to Si-based anode materials. The ion/electron-transfer capability was hierarchically boosted during the redox reaction by manipulating the charge distribution in a specific multi-interface configuration. As a result, this strategy of optimizing the charge-transfer kinetics obtained extraordinary electrochemical properties with excellent rate capability and structural stability in the half/full cell tests. This study has great potential for the preparation of other high-efficiency electrodes for advanced Li-ion storage.

EXPERIMENTS AND METHODS

Preparation of SiO_x@Si Nanoparticles. A 0.8 g amount of commercial Si particles (99.9% metals basis, <50 nm, Macklin) was dispersed into a 40 mL piranha solution (H_2SO_4/H_2O_2 = 7:3 v/v) and continuously stirred magnetically for 2 h at 80 °C. The modified products were centrifuged and rinsed using deionized water and ethanol and then dried in a vacuum oven at 60 °C for 12 h.[6]

Preparation of the C-SiO_x@Si/rGO Composite. The as-prepared SiO_x@Si powder (0.4 g) was dispensed into an ethanol (40 mL) and deionized water (15 mL) mixture, and then ultrasonication was performed for 2 h. Subsequently, $(NH_4)_2S_2O_3$ (0.2 g) was added to the as-prepared dispersions with forceful stirring, and solution A was obtained through sonication sequentially for 3 h. Graphite oxide powder was prepared from natural graphite powder by a modified Hummers method.[55] The β-CD@GO supramolecular colloid B was obtained by initially adding GO (0.13 g) to 100 mL of distilled water. After full sonication, β-CD (0.2 g) was added and kept at 25 °C while being vigorously stirred for 3 h, to initiate the self-assembly process.[12] Afterward, the as-prepared β-CD@GO colloid B was added dropwise to solution A and thoroughly stirred for 2 h to produce a uniform dispersed sol system. The as-prepared mixture was transferred into a polytetrafluoroethylene-lined autoclave for a hydrothermal reaction at 180 °C for 12 h. After being cooled to ambient temperature, the mixture was dried at 90 °C for 18 h to remove ethanol and water. Finally, the material was transferred into a tube furnace and calcined at 600 °C for 3 h at a heat rate of 2 °C min^{-1} (Ar, 60 mL min^{-1}). Then, 10% hydrofluoric acid (HF) was used to etch the product for 30 s to obtain a C-SiO_x@Si/rGO composite. The targeted Si content in the composite was 70−80 wt %. Additionally, the as-prepared sample without β-CD was denoted as SiO_x@Si/rGO.

Material Characterization. The morphology and cross-sectional properties of the samples were analyzed using an SEM (Gemini 500) and a TEM (FEI F30). The EDX spectroscopy of the C-SiO_x@Si/rGO composite was observed using a Talos TEM (FEI, Talos F200X). The XRD was measured using an X-ray generator from 10° to 80° (Cu Kα radiation, λ = 1.5418 Å). The Raman analysis was performed with a Renishaw InVia Raman microscope (λ = 633 nm). The EPR tests were performed on the X-band with a 1.00 G modulation amplitude. TGA (STA409PC) was performed in an air atmosphere from 30 to 700 °C. XPS measurements were performed using an ESCALab250Xi apparatus to analyze the chemical states. FTIR spectra were recorded on a Nicolet 750 spectrometer. The thickness of rGO was obtained using atomic force microscopy (SPM-9500J3). The N_2 adsorption/desorption measurements were evaluated at 77 K (ASAP-2020).

Electrochemical Measurement. The electrochemical properties of the as-prepared materials were evaluated by assembling CR2032 coin-type half/full cells. The anode electrode was fabricated by mixing 70 wt % active material, 20 wt % sodium alginate, and 10 wt % acetylene black in deionized water. The resulting slurries were pasted onto a Cu foil and dried in a vacuum oven at 65 °C overnight. The working electrodes were obtained by tailoring discs (12 mm) from the electrode film and pressed (the electrode thickness is ~10 μm). The electrolyte solution was 1 M $LiPF_6$ in EC/DMC (v/v = 1:1) with 5 wt % fluoroethylene carbonate additive. The metallic Li foil and Celgard 2400 membrane were selected as the counter-electrode and separator, respectively. The mass loading of the active material was 0.4−0.8 mg cm^{-2}, which is enough to match the capacity of the cathode. The assembly processes of the cells were conducted in an Ar-filled glovebox, followed by aging for at least 24 h before performing the electrochemical performance tests.

The full cells comprised commercial NCM (Kejing Star Technology Co., Ltd., Shenzhen) as the cathode and C-SiO_x@Si/rGO composite as the anode. The anode was prelithiated by adding a few drops of electrolyte on the C-SiO_x@Si/rGO electrode and pressing with Li foil for 20 min. The mass ratio of the cathode and anode was set at 10:1. The specific capacities of the full cell were calculated based on the total weight of the active materials.

The GITT measurements were conducted on a Land 2001A battery tester from 0.01 to 2.0 V. The full cell was charged/discharged over a voltage range of 2.8−4.5 V. CV curves were recorded using a CHI660E electrochemical workstation from 0.01 to 2.0 V and 2.8 to 4.5 V for a half and full cell, respectively. EIS was measured using the CHI660E workstation with an applied voltage amplitude of 5 mV (0.01 Hz to 100 kHz).

Theoretical Calculations. All periodic boundary condition density functional theory calculations in this study were executed by employing the Vienna *ab initio* simulation program package (VASP version 5.4.1).[56−58] The Kohn−Sham equations were solved *via* a plane-wave basis set through the projector-augmented wave method. Pseudopotentials were composed of PAW_PBE C, N, O, S, and Si. To simplify the calculations and save time, SiO_2 was used to replace

https://dx.doi.org/10.1021/acsnano.0c01796
ACS Nano 2020, 14, 7066−7076

SiO_x for all corresponding theoretical simulation calculations.[6] The crystal rGO, Si, and SiO_2 are taken as the conventional standards. All heterostructures were constructed using the VASPKIT package with the mismatch error within 3%. The K-points were $3 \times 3 \times 1$.[59]

The corresponding interaction energy (E) was calculated using the following equation (AA represents alginic acid):

$$E = E(\text{AA-rGO-SiO}_x) - E(\text{AA}) - E(\text{rGO}) - E(\text{SiO}_x) \quad (2)$$

The charge density difference is defined as follows:

For the SiO_x@Si model:

$$\Delta\rho(\text{SiO}_x//\text{Si}) = \rho(\text{SiO}_x@\text{Si}) - \rho(\text{SiO}_x) - \rho(\text{Si}) \quad (3)$$

For the SiOx/rGO model:

$$\Delta\rho(\text{SiO}_x//\text{rGO}) = \rho(\text{SiO}_x/\text{rGO}) - \rho(\text{SiO}_x) - \rho(\text{rGO}) \quad (4)$$

For C-SiO_x@Si/rGO model: There are two interfaces in the C-SiO_x@Si/rGO composite, namely, Si//SiO_x and SiO_x//rGO. The charge difference at the Si//SiO_x interface in the composite was built as an entire model using SiO_x and rGO:

$$\Delta\rho(\text{SiO}_x//\text{Si}) = \rho(\text{C-SiO}_x@\text{Si/rGO}) - \rho(\text{SiO}_x/\text{rGO}) - \rho(\text{Si}) \quad (5)$$

Similarly, SiO_x and Si were constructed as an entire model to obtain the charge difference at the SiO_x//rGO interface in the composite, with the corresponding charge density difference formula:

$$\Delta\rho(\text{SiO}_x//\text{rGO}) = \rho(\text{C-SiO}_x@\text{Si/rGO}) - \rho(\text{SiO}_x@\text{Si}) - \rho(\text{rGO}) \quad (6)$$

ASSOCIATED CONTENT

Supporting Information

The Supporting Information is available free of charge at https://pubs.acs.org/doi/10.1021/acsnano.0c01796.

Additional experimental data, including the FTIR spectrum of SiO_x@Si, β-CD, and β-CD/SiO_x@Si; SEM of SiO_x@Si and SiO_x@Si/rGO; TEM with SEAD of SiO_x@Si and SiO_x@Si/rGO; XPS of different samples; EPR of different samples; SEM of the SiO_x@Si electrode after cycling; Raman spectra of the C-SiO_x@Si/rGO electrode after cycling; schematic illustration of the evolution of SiO_x@Si and C-SiO_x@Si/rGO electrodes during cycling; schematic diagram of the configuration of the full cell and the prelithiated process, and the electrochemical performance of different electrodes (PDF)

AUTHOR INFORMATION

Corresponding Authors

Feng Long Gu − *Key Laboratory of Theoretical Chemistry of Environment, Ministry of Education, School of Chemistry, South China Normal University, Guangzhou 510006, People's Republic of China*; Email: gu@scnu.edu.cn

Yexiang Tong − *MOE of the Key Laboratory of Bioinorganic and Synthetic Chemistry, The Key Lab of Low-Carbon Chemistry & Energy Conservation of Guangdong Province, School of Chemistry, Sun Yat-sen University, Guangzhou 510275, People's Republic of China*; orcid.org/0000-0003-4344-443X; Email: chedhx@mail.sysu.edu.cn

Authors

Tao Meng − *MOE of the Key Laboratory of Bioinorganic and Synthetic Chemistry, The Key Lab of Low-Carbon Chemistry & Energy Conservation of Guangdong Province, School of Chemistry, Sun Yat-sen University, Guangzhou 510275, People's Republic of China*

Bo Li − *Key Laboratory of Theoretical Chemistry of Environment, Ministry of Education, School of Chemistry, South China Normal University, Guangzhou 510006, People's Republic of China*; orcid.org/0000-0002-2961-2874

Qiushi Wang − *MOE of the Key Laboratory of Bioinorganic and Synthetic Chemistry, The Key Lab of Low-Carbon Chemistry & Energy Conservation of Guangdong Province, School of Chemistry, Sun Yat-sen University, Guangzhou 510275, People's Republic of China*

Junnan Hao − *Institute for Superconducting & Electronic Materials, School of Mechanical, Materials and Mechatronics Engineering, University of Wollongong, Wollongong, NSW 2522, Australia*

Binbin Huang − *MOE of the Key Laboratory of Bioinorganic and Synthetic Chemistry, The Key Lab of Low-Carbon Chemistry & Energy Conservation of Guangdong Province, School of Chemistry, Sun Yat-sen University, Guangzhou 510275, People's Republic of China*

Huimin Xu − *MOE of the Key Laboratory of Bioinorganic and Synthetic Chemistry, The Key Lab of Low-Carbon Chemistry & Energy Conservation of Guangdong Province, School of Chemistry, Sun Yat-sen University, Guangzhou 510275, People's Republic of China*

Peng Liu − *MOE of the Key Laboratory of Bioinorganic and Synthetic Chemistry, The Key Lab of Low-Carbon Chemistry & Energy Conservation of Guangdong Province, School of Chemistry, Sun Yat-sen University, Guangzhou 510275, People's Republic of China*

Complete contact information is available at: https://pubs.acs.org/10.1021/acsnano.0c01796

Notes

The authors declare no competing financial interest.

ACKNOWLEDGMENTS

This work was supported by the National Key R&D Program of China (2016YFA0202604), the National Natural Science Foundation of China (21773315), the Local Innovative and Research Teams Project of Guangdong Pearl River Talents Program, the National Natural Science Foundation of China (21673085), the Guangdong-Hong Kong Technology Cooperation Funding Scheme (2017A050506048), and the Fundamental Research Funds for the Central Universities (31000-31610782).

REFERENCES

(1) Li, M.; Lu, J.; Chen, Z.; Amine, K. 30 Years of Lithium-Ion Batteries. *Adv. Mater.* **2018**, *30*, 1800561.

(2) Li, P.; Zhao, G.; Zheng, X.; Xu, X.; Yao, C.; Sun, W.; Dou, S. X. Recent Progress on Silicon-Based Anode Materials for Practical Lithium-Ion Battery Applications. *Energy Storage Mater.* **2018**, *15*, 422−446.

(3) Wu, J.; Ma, F.; Liu, X.; Fan, X.; Shen, L.; Wu, Z.; Ding, X.; Han, X.; Deng, Y.; Hu, W.; Zhong, C. Recent Progress in Advanced Characterization Methods for Silicon-Based Lithium-Ion Batteries. *Small Methods* **2019**, *3*, 1900158.

(4) Zhao, C.; Wada, T.; De Andrade, V.; Gürsoy, D.; Kato, H.; Chen-Wiegart, Y.-c. K. Imaging of 3D Morphological Evolution of Nanoporous Silicon Anode in Lithium Ion Battery by X-Ray Nano-Tomography. *Nano Energy* **2018**, *52*, 381−390.
(5) Shang, H.; Zuo, Z.; Yu, L.; Wang, F.; He, F.; Li, Y. Low-Temperature Growth of All-Carbon Graphdiyne on a Silicon Anode for High-Performance Lithium-Ion Batteries. *Adv. Mater.* **2018**, *30*, 1801459.
(6) Guo, S.; Li, H.; Li, Y.; Han, Y.; Chen, K.; Xu, G.; Zhu, Y.; Hu, X. SiO_2-Enhanced Structural Stability and Strong Adhesion with a New Binder of Konjac Glucomannan Enables Stable Cycling of Silicon Anodes for Lithium-Ion Batteries. *Adv. Energy Mater.* **2018**, *8*, 1800434.
(7) Cao, Y.; Fatemi, V.; Fang, S.; Watanabe, K.; Taniguchi, T.; Kaxiras, E.; Jarillo-Herrero, P. Unconventional Superconductivity in Magic-Angle Graphene Superlattices. *Nature* **2018**, *556*, 43.
(8) Ji, J.; Ji, H.; Zhang, L. L.; Zhao, X.; Bai, X.; Fan, X.; Zhang, F.; Ruoff, R. S. Graphene-Encapsulated Si on Ultrathin-Graphite Foam as Anode for High Capacity Lithium-Ion Batteries. *Adv. Mater.* **2013**, *25*, 4673−4677.
(9) Li, Y.; Yan, K.; Lee, H.-W.; Lu, Z.; Liu, N.; Cui, Y. Growth of Conformal Graphene Cages on Micrometre-Sized Silicon Particles as Stable Battery Anodes. *Nat. Energy* **2016**, *1*, 15029.
(10) Balogun, M.-S.; Yang, H.; Luo, Y.; Qiu, W.; Huang, Y.; Liu, Z.-Q.; Tong, Y. Achieving High Gravimetric Energy Density for Flexible Lithium-Ion Batteries Facilitated by Core-Double-Shell Electrodes. *Energy Environ. Sci.* **2018**, *11*, 1859−1869.
(11) Yan, C.; Zhu, Y.; Li, Y.; Fang, Z.; Peng, L.; Zhou, X.; Chen, G.; Yu, G. Local Built-In Electric Field Enabled in Carbon-Doped Co_3O_4 Nanocrystals for Superior Lithium-Ion Storage. *Adv. Funct. Mater.* **2018**, *28*, 1705951.
(12) Huang, Y.; Gao, A.; Song, X.; Shu, D.; Yi, F.; Zhong, J.; Zeng, R.; Zhao, S.; Meng, T. Supramolecule-Inspired Fabrication of Carbon Nanoparticles *In Situ* Anchored Graphene Nanosheets Material for High-Performance Supercapacitors. *ACS Appl. Mater. Interfaces* **2016**, *8*, 26775−26782.
(13) Lagrost, C.; Alcaraz, G.; Bergamini, J.-F.; Fabre, B.; Serbanescu, I. Functionalization of Silicon Surfaces with Si-C Linked *β*-Cyclodextrin Monolayers. *Chem. Commun.* **2007**, 1050−1052.
(14) Ghosh, S.; Badruddoza, A.; Uddin, M.; Hidajat, K. Adsorption of Chiral Aromatic Amino Acids onto Carboxymethyl-*β*-Cyclodextrin Bonded Fe_3O_4/SiO_2 Core-Shell Nanoparticles. *J. Colloid Interface Sci.* **2011**, *354*, 483−492.
(15) Jeong, Y. K.; Kwon, T.-w.; Lee, I.; Kim, T.-S.; Coskun, A.; Choi, J. W. Hyperbranched *β*-Cyclodextrin Polymer as an Effective Multidimensional Binder for Silicon Anodes in Lithium Rechargeable Batteries. *Nano Lett.* **2014**, *14*, 864−870.
(16) Fu, R.; Zhang, K.; Zaccaria, R. P.; Huang, H.; Xia, Y.; Liu, Z. Two-Dimensional Silicon Suboxides Nanostructures with Si Nano-domains Confined in Amorphous SiO_2 Derived from Siloxene as High Performance Anode for Li-Ion Batteries. *Nano Energy* **2017**, *39*, 546−553.
(17) Li, L.; Zuo, Z.; Shang, H.; Wang, F.; Li, Y. *In-Situ* Constructing 3D Graphdiyne as All-Carbon Binder for High-Performance Silicon Anode. *Nano Energy* **2018**, *53*, 135−143.
(18) Lin, L.; Xu, X.; Chu, C.; Majeed, M. K.; Yang, J. Mesoporous Amorphous Silicon: A Simple Synthesis of a High-Rate and Long-Life Anode Material for Lithium-Ion Batteries. *Angew. Chem., Int. Ed.* **2016**, *55*, 14063−14066.
(19) Meng, T.; Li, B.; Hu, L.; Yang, H.; Fan, W.; Zhang, S.; Liu, P.; Li, M.; Gu, F. L.; Tong, Y. Engineering of Oxygen Vacancy and Electric-Field Effect by Encapsulating Lithium Titanate in Reduced Graphene Oxide for Superior Lithium Ion Storage. *Small Methods* **2019**, *3*, 1900185.
(20) Zheng, Y.; Zhou, T.; Zhao, X.; Pang, W. K.; Gao, H.; Li, S.; Zhou, Z.; Liu, H.; Guo, Z. Atomic Interface Engineering and Electric-Field Effect in Ultrathin Bi_2MoO_6 Nanosheets for Superior Lithium Ion Storage. *Adv. Mater.* **2017**, *29*, 1700396.
(21) Long, B.; Yang, H.; Li, M.; Balogun, M.-S.; Mai, W.; Ouyang, G.; Tong, Y.; Tsiakaras, P.; Song, S. Interface Charges Redistribution Enhanced Monolithic Etched Copper Foam-Based Cu_2O Layer/TiO_2 Nanodots Heterojunction with High Hydrogen Evolution Electrocatalytic Activity. *Appl. Catal., B* **2019**, *243*, 365−372.
(22) Jahan, M.; Li, K.; Zhao, G. L. Electric Field Poling Effect on the Electrocatalytic Properties of Nitrogen-Functionalized Graphene Nanosheets. *Energy Technol-Ger* **2018**, *6*, 2408−2418.
(23) Wang, X.; Li, G.; Seo, M. H.; Hassan, F. M.; Hoque, M. A.; Chen, Z. Sulfur Atoms Bridging Few-Layered MoS_2 with S-Doped Graphene Enable Highly Robust Anode for Lithium-Ion Batteries. *Adv. Energy Mater.* **2015**, *5*, 1501106.
(24) Qu, L.; Liu, Y.; Baek, J.-B.; Dai, L. Nitrogen-Doped Graphene as Efficient Metal-Free Electrocatalyst for Oxygen Reduction in Fuel Cells. *ACS Nano* **2010**, *4*, 1321−1326.
(25) Reddy, A. L. M.; Srivastava, A.; Gowda, S. R.; Gullapalli, H.; Dubey, M.; Ajayan, P. M. Synthesis of Nitrogen-Doped Graphene Films for Lithium Battery Application. *ACS Nano* **2010**, *4*, 6337−6342.
(26) Hao, J.; Zhang, J.; Xia, G.; Liu, Y.; Zheng, Y.; Zhang, W.; Tang, Y.; Pang, W. K.; Guo, Z. Heterostructure Manipulation *via In Situ* Localized Phase Transformation for High-Rate and Highly Durable Lithium Ion Storage. *ACS Nano* **2018**, *12*, 10430−10438.
(27) Ye, K.; Li, Y.; Yang, H.; Li, M.; Huang, Y.; Zhang, S.; Ji, H. An Ultrathin Carbon Layer Activated CeO_2 Heterojunction Nanorods for Photocatalytic Degradation of Organic Pollutants. *Appl. Catal., B* **2019**, *259*, 118085.
(28) Su, H.; Barragan, A. A.; Geng, L.; Long, D.; Ling, L.; Bozhilov, K. N.; Mangolini, L.; Guo, J. Colloidal Synthesis of Silicon-Carbon Composite Material for Lithium-Ion Batteries. *Angew. Chem.* **2017**, *129*, 10920−10925.
(29) Xu, Q.; Sun, J. K.; Yu, Z. L.; Yin, Y. X.; Xin, S.; Yu, S. H.; Guo, Y. G. SiO_x Encapsulated in Graphene Bubble Film: An Ultrastable Li-Ion Battery Anode. *Adv. Mater.* **2018**, *30*, 1707430.
(30) Li, N.; Jin, S.; Liao, Q.; Cui, H.; Wang, C. Encapsulated within Graphene Shell Silicon Nanoparticles Anchored on Vertically Aligned Graphene Trees as Lithium Ion Battery Anodes. *Nano Energy* **2014**, *5*, 105−115.
(31) Huang, X.; Yang, J.; Mao, S.; Chang, J.; Hallac, P. B.; Fell, C. R.; Metz, B.; Jiang, J.; Hurley, P. T.; Chen, J. Controllable Synthesis of Hollow Si Anode for Long-Cycle-Life Lithium-Ion Batteries. *Adv. Mater.* **2014**, *26*, 4326−4332.
(32) Liu, Z.; Zhao, Y.; He, R.; Luo, W.; Meng, J.; Yu, Q.; Zhao, D.; Zhou, L.; Mai, L. Yolk@Shell SiO_x/C Microspheres with Semi-Graphitic Carbon Coating on the Exterior and Interior Surfaces for Durable Lithium Storage. *Energy Storage Mater.* **2019**, *19*, 299−305.
(33) Deng, J.; Ji, H.; Yan, C.; Zhang, J.; Si, W.; Baunack, S.; Oswald, S.; Mei, Y.; Schmidt, O. G. Naturally Rolled-Up C/Si/C Trilayer Nanomembranes as Stable Anodes for Lithium-Ion Batteries with Remarkable Cycling Performance. *Angew. Chem., Int. Ed.* **2013**, *52*, 2326−2330.
(34) Li, H.; Yu, H.; Zhang, X.; Guo, G.; Hu, J.; Dong, A.; Yang, D. Bowl-like 3C-SiC Nanoshells Encapsulated in Hollow Graphitic Carbon Spheres for High-Rate Lithium-Ion Batteries. *Chem. Mater.* **2016**, *28*, 1179−1186.
(35) Chen, Y.; Liu, L.; Xiong, J.; Yang, T.; Qin, Y.; Yan, C. Porous Si Nanowires from Cheap Metallurgical Silicon Stabilized by a Surface Oxide Layer for Lithium Ion Batteries. *Adv. Funct. Mater.* **2015**, *25*, 6701−6709.
(36) Zhang, L.; Rajagopalan, R.; Guo, H.; Hu, X.; Dou, S.; Liu, H. A Green and Facile Way to Prepare Granadilla-Like Silicon-Based Anode Materials for Li-Ion Batteries. *Adv. Funct. Mater.* **2016**, *26*, 440−446.
(37) Zhang, Z.; Wang, Y.; Ren, W.; Tan, Q.; Chen, Y.; Li, H.; Zhong, Z.; Su, F. Scalable Synthesis of Interconnected Porous Silicon/Carbon Composites by the Rochow Reaction as High-Performance Anodes of Lithium Ion Batteries. *Angew. Chem.* **2014**, *126*, 5265−5269.

https://dx.doi.org/10.1021/acsnano.0c01796
ACS Nano 2020, 14, 7066−7076

(38) Fu, R.; Zhang, K.; Zaccaria, R. P.; Huang, H.; Xia, Y.; Liu, Z. Two-Dimensional Silicon Suboxides Nanostructures with Si Nanodomains Confined in Amorphous SiO_2 Derived from Siloxene as High Performance Anode for Li-Ion Batteries. *Nano Energy* **2017**, *39*, 546–553.
(39) Hao, J.; Long, J.; Li, B.; Li, X.; Zhang, S.; Yang, F.; Zeng, X.; Yang, Z.; Pang, W. K.; Guo, Z. Toward High-Performance Hybrid Zn-Based Batteries *via* Deeply Understanding Their Mechanism and Using Electrolyte Additive. *Adv. Funct. Mater.* **2019**, *29*, 1903605.
(40) Luo, W.; Li, F.; Li, Q.; Wang, X.; Yang, W.; Zhou, L.; Mai, L. Heterostructured Bi_2S_3-Bi_2O_3 Nanosheets with a Built-In Electric Field for Improved Sodium Storage. *ACS Appl. Mater. Interfaces* **2018**, *10*, 7201–7207.
(41) Meng, T.; Hao, Y.-N.; Qin, J.; Cao, M. Interface-Engineering-Induced Electric Field Effect and Atomic Disorder in Cobalt Selenide for High-Rate and Large-Capacity Lithium Storage. *ACS Sustainable Chem. Eng.* **2019**, *7*, 4657–4665.
(42) Liu, Y.; Zhou, T.; Zheng, Y.; He, Z.; Xiao, C.; Pang, W. K.; Tong, W.; Zou, Y.; Pan, B.; Guo, Z. Local Electric Field Facilitates High-Performance Li-Ion Batteries. *ACS Nano* **2017**, *11*, 8519–8526.
(43) Li, K.; Lu, X.; Zhang, Y.; Liu, K.; Huang, Y.; Liu, H. Bi_3TaO_7/Ti_3C_2 Heterojunctions for Enhanced Photocatalytic Removal of Water-Borne Contaminants. *Environ. Res.* **2020**, *185*, 109409.
(44) Zheng, Y.; Zhou, T.; Zhang, C.; Mao, J.; Liu, H.; Guo, Z. Boosted Charge Transfer in SnS/SnO_2 Heterostructures: Toward High Rate Capability for Sodium-Ion Batteries. *Angew. Chem., Int. Ed.* **2016**, *55*, 3408–3413.
(45) Liu, Y.; Tai, Z.; Zhou, T.; Sencadas, V.; Zhang, J.; Zhang, L.; Konstantinov, K.; Guo, Z.; Liu, H. K. An All-Integrated Anode *via* Interlinked Chemical Bonding between Double-Shelled-Yolk-Structured Silicon and Binder for Lithium-Ion Batteries. *Adv. Mater.* **2017**, *29*, 1703028.
(46) Choi, C.; Ashby, D. S.; Butts, D. M.; DeBlock, R. H.; Wei, Q.; Lau, J.; Dunn, B. Achieving High Energy Density and High Power Density with Pseudocapacitive Materials. *Nat. Rev. Mater.* **2020**, *5*, 1–15.
(47) Salvatierra, R. V.; Raji, A. R. O.; Lee, S. K.; Ji, Y.; Li, L.; Tour, J. M. Silicon Nanowires and Lithium Cobalt Oxide Nanowires in Graphene Nanoribbon Papers for Full Lithium Ion Battery. *Adv. Energy Mater.* **2016**, *6*, 1600918.
(48) Zhang, Q.; Chen, H.; Luo, L.; Zhao, B.; Luo, H.; Han, X.; Wang, J.; Wang, C.; Yang, Y.; Zhu, T. Harnessing the Concurrent Reaction Dynamics in Active Si and Ge to Achieve High Performance Lithium-Ion Batteries. *Energy Environ. Sci.* **2018**, *11*, 669–681.
(49) Chen, S.; Shen, L.; van Aken, P. A.; Maier, J.; Yu, Y. Dual-Functionalized Double Carbon Shells Coated Silicon Nanoparticles for High Performance Lithium-Ion Batteries. *Adv. Mater.* **2017**, *29*, 1605650.
(50) Zhou, X.; Yu, Y.; Yang, J.; Wang, H.; Jia, M.; Tang, J. Cross-Linking Tin-Based Metal-Organic Frameworks with Encapsulated Silicon Nanoparticles: High-Performance Anodes for Lithium-Ion Batteries. *ChemElectroChem* **2019**, *6*, 2056–2063.
(51) Liu, Z.; Guan, D.; Yu, Q.; Xu, L.; Zhuang, Z.; Zhu, T.; Zhao, D.; Zhou, L.; Mai, L. Monodisperse and Homogeneous SiO_x/C Microspheres: A Promising High-Capacity and Durable Anode Material for Lithium-Ion Batteries. *Energy Storage Mater.* **2018**, *13*, 112–118.
(52) Yi, Z.; Qian, Y.; Cao, C.; Lin, N.; Qian, Y. Porous Si/C Microspheres Decorated with Stable Outer Carbon Interphase and Inner Interpenetrated Si@C Channel for Enhanced Lithium Storage. *Carbon* **2019**, *149*, 664–671.
(53) Fridman, K.; Sharabi, R.; Markevich, E.; Elazari, R.; Salitra, G.; Gershinsky, G.; Aurbach, D.; Lampert, J.; Schulz-Dobrick, M. An Advanced Lithium Ion Battery Based on Amorphous Silicon Film Anode and Integrated xLi_2MnO_3.(1-x) $LiNi_yMn_zCo_{1-y-z}O_2$ Cathode. *ECS Electrochem. Lett.* **2013**, *2*, A84–A87.
(54) Fridman, K.; Sharabi, R.; Elazari, R.; Gershinsky, G.; Markevich, E.; Salitra, G.; Aurbach, D.; Garsuch, A.; Lampert, J. A New Advanced Lithium Ion Battery: Combination of High Performance Amorphous Columnar Silicon Thin Film Anode, 5V $LiNi_{0.5}Mn_{1.5}O_4$ Spinel Cathode and Fluoroethylene Carbonate-Based Electrolyte Solution. *Electrochem. Commun.* **2013**, *33*, 31–34.
(55) Zhang, F.; Yi, F.; Meng, T.; Gao, A.; Shu, D.; Chen, H.; Cheng, H.; Zhou, X. *In Situ* Supramolecular Self-Assembly Assisted Synthesis of $Li_4Ti_5O_{12}$-Carbon-Reduced Graphene Oxide Microspheres for Lithium-Ion Batteries. *ACS Sustainable Chem. Eng.* **2019**, *7*, 916–924.
(56) Kresse, G.; Hafner, J. *Ab Initio* Molecular Dynamics for Liquid Metals. *Phys. Rev. B: Condens. Matter Mater. Phys.* **1993**, *47*, 558.
(57) Kresse, G.; Hafner, J. *Ab Initio* Molecular-Dynamics Simulation of the Liquid-Metal-Amorphous-Semiconductor Transition in Germanium. *Phys. Rev. B: Condens. Matter Mater. Phys.* **1994**, *49*, 14251–14269.
(58) Kresse, G.; Furthmüller, J. Efficient Iterative Schemes for *Ab Initio* Total-Energy Calculations Using a Plane-Wave Basis Set. *Phys. Rev. B: Condens. Matter Mater. Phys.* **1996**, *54*, 11169.
(59) Wang, V.; Xu, N.; Liu, J.-C; Tang, G.; Geng, W. VASPKIT: A Pre-and Post-Processing Program for VASP Code. 2020, arXiv:1908.08269v4 [cond-mat.mtrl-sci]. *ChemRxiv*. https://arxiv.org/abs/1908.08269 (accessed February 22, 2020).

https://dx.doi.org/10.1021/acsnano.0c01796
ACS Nano 2020, 14, 7066–7076